

# Correspondence

## Three-Dimensional Registration and Fusion of Ultrasound and MRI Using Major Vessels as Fiducial Markers

Brian C. Porter, Deborah J. Rubens, John G. Strang, Jason Smith, Saara Totterman, and Kevin J. Parker\*

**Abstract**—This paper describes fusion of three-dimensional (3-D) ultrasound (US) and magnetic resonance imaging (MRI) data sets, without the assistance of external fiducial markers or external position sensors. Fusion of these two modalities combines real-time 3-D ultrasound scans of soft tissue with the larger anatomical framework from MRI. The complementary information available from multiple imaging modalities warrants the development of robust fusion capabilities. We describe the data acquisition, specialized algorithms, and results for 3-D fused data from phantom studies and *in vivo* studies of the normal human vasculature and musculoskeletal systems.

**Index Terms**—Image fusion, MRI, 3-D imaging, ultrasound, voxel.

### I. INTRODUCTION

Three-dimensional (3-D) data acquisition is well established for magnetic resonance imaging (MRI) and more recently for ultrasound (US). In simplest implementation, 3-D image information can be obtained from a sequential series of two-dimensional (2-D) tomographic images taken over a volume. The goal of multimodality image registration (3-D alignment) and fusion (data merging) is well established in certain areas where complementary information can be obtained. In this paper, *fusion* refers to the entire process of registration and combination of data for visualization. We focus on the fusion of 3-D MRI and US information with the long term goal of gaining complementary information in a way that enhances the clinical usefulness of these modalities. Potential uses for merged or fused 3-D images include the placement of liver tumor information from MRI into US for subsequent biopsy or therapy; and the fusion of high-resolution volume MRI of brain, liver or renal lesions with US-guided tumor resection or ablation.

Fusion techniques generally fall into one of two categories: framed fusion or frameless fusion [1]. Framed fusion uses external frames, bony landmarks (such as the skull) or manually placed fiducial markers to match complementary data sets. Frameless fusion of soft tissue may use organ surfaces and vascular structures to align image volumes. Our study investigates a new fusion method using vessels segmented from 3-D MRI and US data. The segmented vessels were used as landmarks within a correlation algorithm to spatially align the two 3-D volumes.

Manuscript received March 29, 1999; revised January 19, 2001. This work was supported in part by the National Institutes of Health (NIH), the Center for Electronic Imaging Systems, the University of Rochester departments of Radiology, Electrical Engineering, and General Electric Corporation. The Associate Editor responsible for coordinating the review of this paper and recommending its publication was M. W. Vannier. *Asterisk indicates corresponding author.*

B. C. Porter and J. Smith are with the Department of Electrical and Computer Engineering, University of Rochester, Rochester, NY 14627 USA.

D. J. Rubens, J. G. Strang, and S. Totterman are with the Department of Radiology, University of Rochester, Rochester, NY 14627 USA

\*K. J. Parker is with the Department of Electrical and Computer Engineering and the Department of Radiology, University of Rochester, Rochester, NY 14627 USA (e-mail: parker@ece.rochester.edu)

Publisher Item Identifier S 0278-0062(01)03554-6.

### II. METHODS

3-D MRI sequences were obtained on a GE Signa 1.5-T unit [General Electric Medical Systems, Milwaukee, WI]. For imaging of the forearm, a surface coil was used. [2-D time-of-flight images using spoiled gradient echo sequence with flow compensation, with 2-mm slice thickness and  $256 \times 128$  matrix and 10-cm field-of-view (FOV) producing  $0.391 \text{ mm} \times 0.782 \text{ mm}$  pixel size in axial and oblique-axial planes] For imaging of the liver, a torso coil was used. [3-D fast gradient echo (efgre3d/15), axial, 1.4-mm interslice spacing, 5.6-mm slice thickness, matrix  $512 \times 512$ ,  $30 \text{ cm} \times 22.5 \text{ cm}$  FOV, pixel size  $0.586 \text{ mm}$ ] For phantom imaging, a quadrilateral head coil was used. [Two-dimensional spin echo images, thickness 2.5-mm contiguous, matrix  $256 \times 256$ ,  $14 \text{ cm} \times 10.5\text{-cm}$  FOV, pixel size  $0.547 \text{ mm}$ ]

Vessels (and vessel-like structures in the phantom) were segmented from MRI volumes using simple threshold in some cases and in other cases using a 3-D region growing segmentation algorithm [2]. The threshold level for a set of images was determined by visual inspection, and the region growing settings were optimized for segmentation of liver tissue, which generated a negative mask for liver vessels. The vessel volumes were stored with 1-mm voxel resolution after interpolating the interslice images and decimating the in-plane images. Fig. 1 shows a 3-D reconstruction of vessels from the left forearm displayed with three intersecting axial slices.

US data were acquired using a GE Logiq 700 ultrasound scanner [GE Medical Systems, Milwaukee, WI] with Extend Research Package. Extend collects image data and saves single frames or CINE loops of b-scan and color flow data. After acquisition, data files were transferred from the US hard disks to a workstation for off-line image processing and analysis.

Volumetric US data was obtained with a motorized track that moves the US transducer at a controlled, uniform speed [Velmetx, Bloomfield, New York]. The track velocity was matched to the Logiq acoustic frame rate to achieve 1-mm or 0.5-mm image spacing. The US CINE data was obtained in a sagittal orientation (forearm) [30 frames for 0.5-mm spacing, 7-MHz b-scan, 5-MHz Color Doppler, 4-cm depth] and oblique-axial orientation (abdomen) [80 frames for 1-mm spacing, 5-MHz b-scan, 4-MHz Color Doppler, 14-cm depth] with an acquisition time ranging from 8 s to 20 s for 30–80 frames. A linear probe (General Electric, 739L, 5- to 10-MHz linear transducer) was used to acquire the arm and prostate phantom data, and a curvilinear probe (General Electric, 548C, 3-MHz to 8-MHz convex transducer) was used to acquire the liver data. A diagram of the motorized track is shown in Fig. 2.

The GE Extend software on the US scanner permitted acquisition of co-registered b-scan, Color or Power Doppler images which were transferred from CINE memory. To create the vessel volumes, the Doppler images were segmented using a color pixel-value threshold. The threshold for each set of Doppler images was selected to eliminate color noise artifacts. The remaining small noise artifacts were removed by closing filters based on erosion and dilation operations ( $3 \times 3$  and  $5 \times 5$  matrix sizes). The set of in-plane images were then decimated to achieve 1-mm pixels and combined to create a volume file with 1-mm voxels. No interslice interpolation was needed because US images were acquired with 1-mm or 0.5-mm interslice spacing. Fig. 3 shows a flowchart of image acquisition and processing steps for MRI and US data.

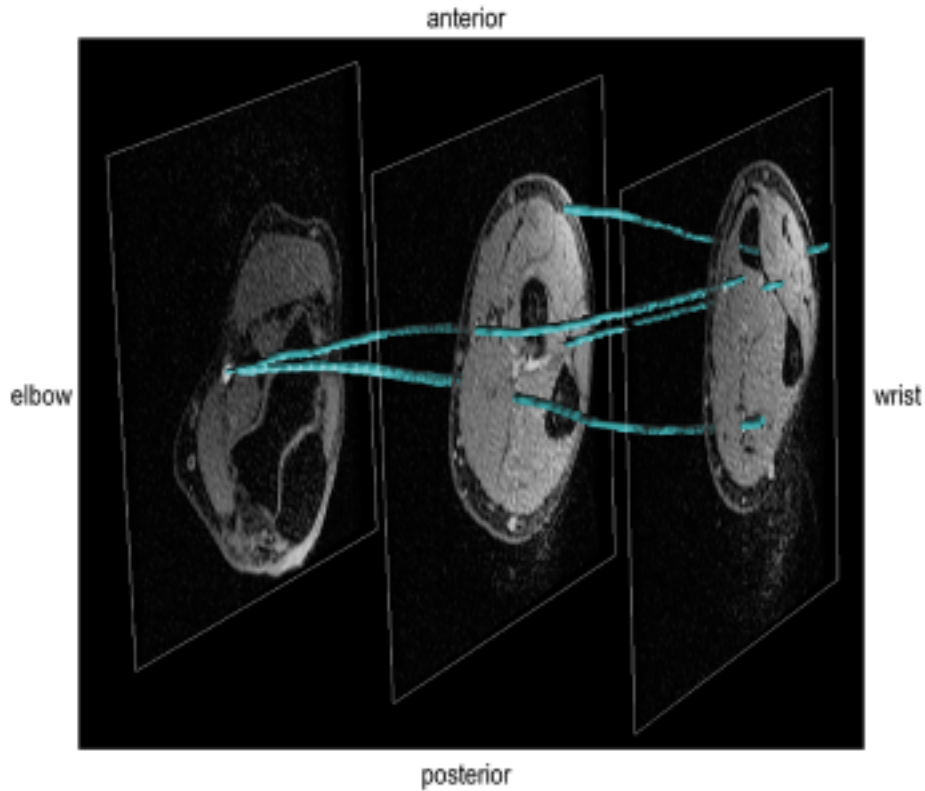


Fig. 1. Segmented vascular MRI of the Arm. Segmented arm vessels (blue) intersect 3 of the axial MRI source images. Bones and subcutaneous tissue are black, muscle gray, and source vessels white.

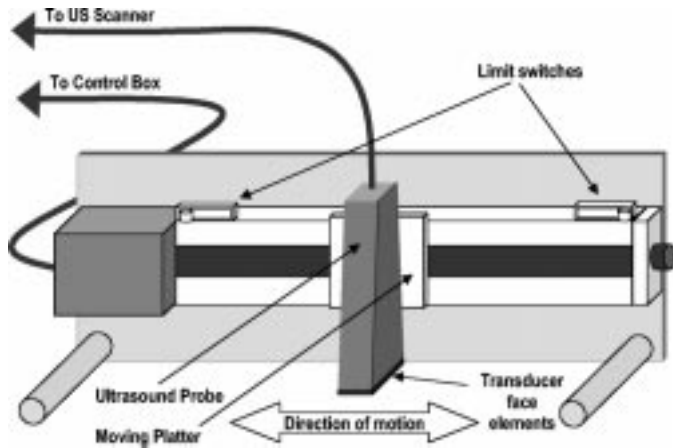


Fig. 2. Motorized track with speed and direction control. Motorized track permits correlation of transducer speed to acoustic frame rate to control the slice thickness and the  $z$  axis distance.

The vessels that are segmented from each data set should have characteristics that allow them to be uniquely oriented in three dimensions. Such features include branching points (bifurcations), natural curvature or multiple vessels. In addition, the same key features should be present in each modality.

**A. Fusion Algorithms**

For fast 3-D visualization and computation, we used IRIS Explorer [Numerical Algorithms Group, Inc., Downers Grove, IL] on a SGI Indigo2. To correlate two volumes, four data sets are needed as input. Two of the four volumes contain original grayscale images, with one

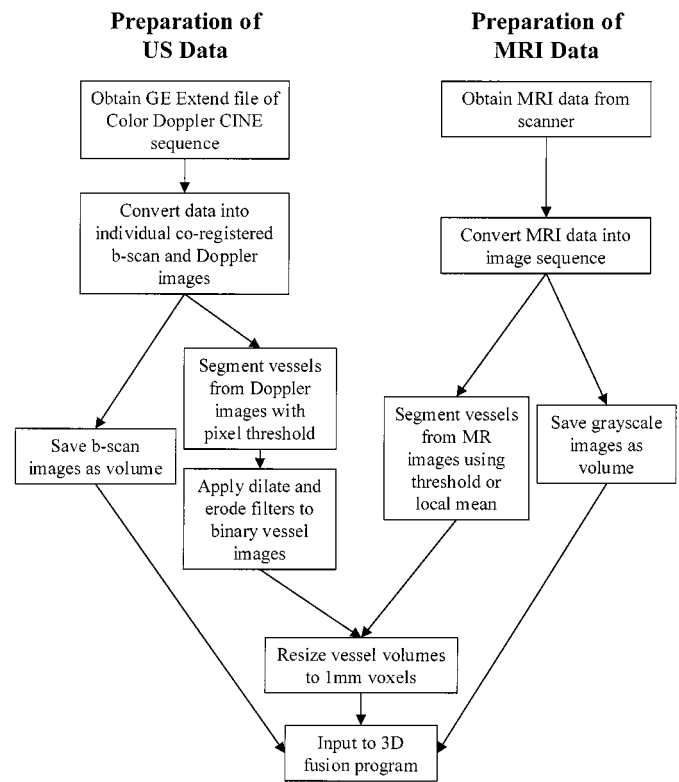


Fig. 3. Image processing flowchart to establish fiducial markers in grayscale volumes.

image set designated as the reference volume. The other two volumes contain the segmented vascular data, scaled to 1-mm voxels.

Fusion was accomplished in a two-step process. The first step was a manual correlation (a fast, user-guided, "coarse adjustment"), and the second was an automated correlation search. The use of a manual step in this process greatly enhances the efficiency and accuracy of the fusion. The MRI data set is fixed in the absolute coordinate system of the Explorer environment and never moved in space. The US data set was selected to be the moveable volume. Using the computer mouse, a user first manually moves the US volume into an overlapping position with the MRI volume, completing a coarse fusion alignment. The user is aided in this alignment procedure by the ability to change the camera angle at which the vessel volumes are viewed. By manipulating the US volume and checking its position with respect to the stationary MRI volume, the user can obtain a coarse approximation to vessel registration. The automated algorithm has successfully registered vessels when the coarse adjustment was up to 20 voxels (mm) offset and  $10^\circ$  rotation about the  $x$ ,  $y$  and  $z$  axes. However, this range may increase or decrease depending on the quality of vessel segmentation.

Once the user positioned the data coarsely, the computer performed an iterative search to determine the highest correlation within a constrained range of motion. This range of motion was predefined by the user as the rotation and translation step-size and maximum rotation angle and translation displacement. The search algorithm implements a 3-D discrete correlation routine for six degrees of freedom in the following order: rotations about  $Z$ - $Y$ - $X$  axes, translations of  $X$ - $Y$ - $Z$ . The highest correlation value calculated for the range of  $Z$  rotations determines the new starting point for a maximum correlation search in  $Y$  rotations, and so on, until the maximum correlation value for the  $Z$  translation is found. The highest correlation value calculated within this limited search, a local maximum, was assumed to be the ideal alignment. The algorithm took from 5 min to 10 min to execute on a SGI Indigo workstation, depending on the range and step size set by the user. After converging upon a solution, the transformation matrix that described the relative positions of these landmark volumes was used to redraw the original grayscale data. Finally, the original images of each modality were aligned and displayed to proper relative scale.

### B. Implementation of Three-Dimensional Correlation

The specifics of the correlation calculation follow: First, since the volume data is represented as a cloud of points, not a mass of connected voxel cubes, one of the data sets needs to be positionally blurred in order to allow information in the two discretized volumes to actually contact one another. The points of the MRI data set were blurred spatially in three dimensions by weighting their input values according to the equation  $(2/3)^R$ , where  $R$  is the voxel distance from the actual data point. The algorithm also restricted this blur to extend only up to eight voxels away in any direction. The blur allows the correlation value to increase as the vessel structures become more closely aligned.

There are three factors that make US data eligible for correlation. First, a point in the US volume must be within eight voxels of a point in the MRI volume. Second, the particular US point must be the closest point to the MRI point under investigation. Third, the US point cannot have been previously chosen for correlation with another MRI point. If a point in the US volume passed these three requirements, it was considered to be eligible and was used in the correlation calculation.

The correlation calculation used in this algorithm is derived from Schwartz's Inequality which states that for two continuous functions  $A$  and  $B$  on their domain  $\omega$

$$\left| \int_{-\infty}^{\infty} A(\omega)B(\omega) d\omega \right|^2 \leq \int_{-\infty}^{\infty} |A(\omega)|^2 d\omega \int_{-\infty}^{\infty} |B(\omega)|^2 d\omega. \quad (1)$$

This relation can be rewritten as

$$\frac{\left| \int_{-\infty}^{\infty} A(\omega)B(\omega) d\omega \right|^2}{\int_{-\infty}^{\infty} |A(\omega)|^2 d\omega \int_{-\infty}^{\infty} |B(\omega)|^2 d\omega} \leq 1. \quad (2)$$

If  $A$  and  $B$  are written as functions of three dimensions, the relation becomes (3), shown at the bottom of the page. In practice, the limits of integration correspond to the spatial extent of the 3-D data. The equation describing a general spatial correlation in three dimensions (Cartesian coordinates) is

$$\begin{aligned} & f(x, y, z) \circ g(x, y, z) \\ &= \int_{-\infty}^{\infty} \int_{-\infty}^{\infty} \int_{-\infty}^{\infty} f^*(\alpha, \beta, \gamma) \\ & \quad \times g(x + \alpha, y + \beta, z + \gamma) d\alpha d\beta d\gamma \end{aligned} \quad (4)$$

where  $f^*$  is the complex conjugate of  $f$ . Notice that if the functions to be correlated,  $f$  and  $g$  are real and nonnegative, as they are in the fusion data sets, then some simplifications can be made, namely

$$\begin{aligned} & f(x, y, z) = f^*(x, y, z) \text{ and} \\ & f(x, y, z) \circ g(x, y, z) = R_{fg}(\Delta x, \Delta y, \Delta z). \end{aligned} \quad (5)$$

Thus, (3) can be rewritten and substituted into an adjusted Schwartz's Inequality as follows:

$$\frac{|R_{fg}(\Delta x, \Delta y, \Delta z)|^2}{R_{ff}(\Delta x, \Delta y, \Delta z)R_{gg}(\Delta x, \Delta y, \Delta z)} \leq 1. \quad (6)$$

As a result, the 3-D cross-correlation function  $R_{fg}$  will produce a correlation value normalized to the product of  $R_{ff}$  and  $R_{gg}$  at each stage in the spatial search for the peak value.

It is important to note that the normalization described in (6) is performed relative to each particular step in the positioning of the volumes, i.e., the meaning of  $R_{ff}$  and  $R_{gg}$  are taken only within the overlap regions of the MRI and US volumes. For example, if the MRI data set (and extracted vessel extent) is much larger than US, only a limited match will necessarily occur and the correlation will be accordingly low. For a valid comparison, the values generated at each position of the volumes are normalized to the peak values of the windowed auto-correlations of both data sets. The normalized equation is

$$\frac{|R_{fg}(\Delta x, \Delta y, \Delta z)|^2}{R_{ff}(0, 0, 0)R_{gg}(0, 0, 0)} \leq 1. \quad (7)$$

The correlation value computed for each new volume position is used to adjust the next position and orientation. During an iterative correlation search, the three rotations are adjusted before the translations in the

$$\frac{\left| \int_{-\infty}^{\infty} \int_{-\infty}^{\infty} \int_{-\infty}^{\infty} A(\alpha, \beta, \gamma)B(\alpha, \beta, \gamma) d\alpha d\beta d\gamma \right|^2}{\int_{-\infty}^{\infty} \int_{-\infty}^{\infty} \int_{-\infty}^{\infty} |A(\alpha, \beta, \gamma)|^2 d\alpha d\beta d\gamma \int_{-\infty}^{\infty} \int_{-\infty}^{\infty} \int_{-\infty}^{\infty} |B(\alpha, \beta, \gamma)|^2 d\alpha d\beta d\gamma} \leq 1 \quad (3)$$

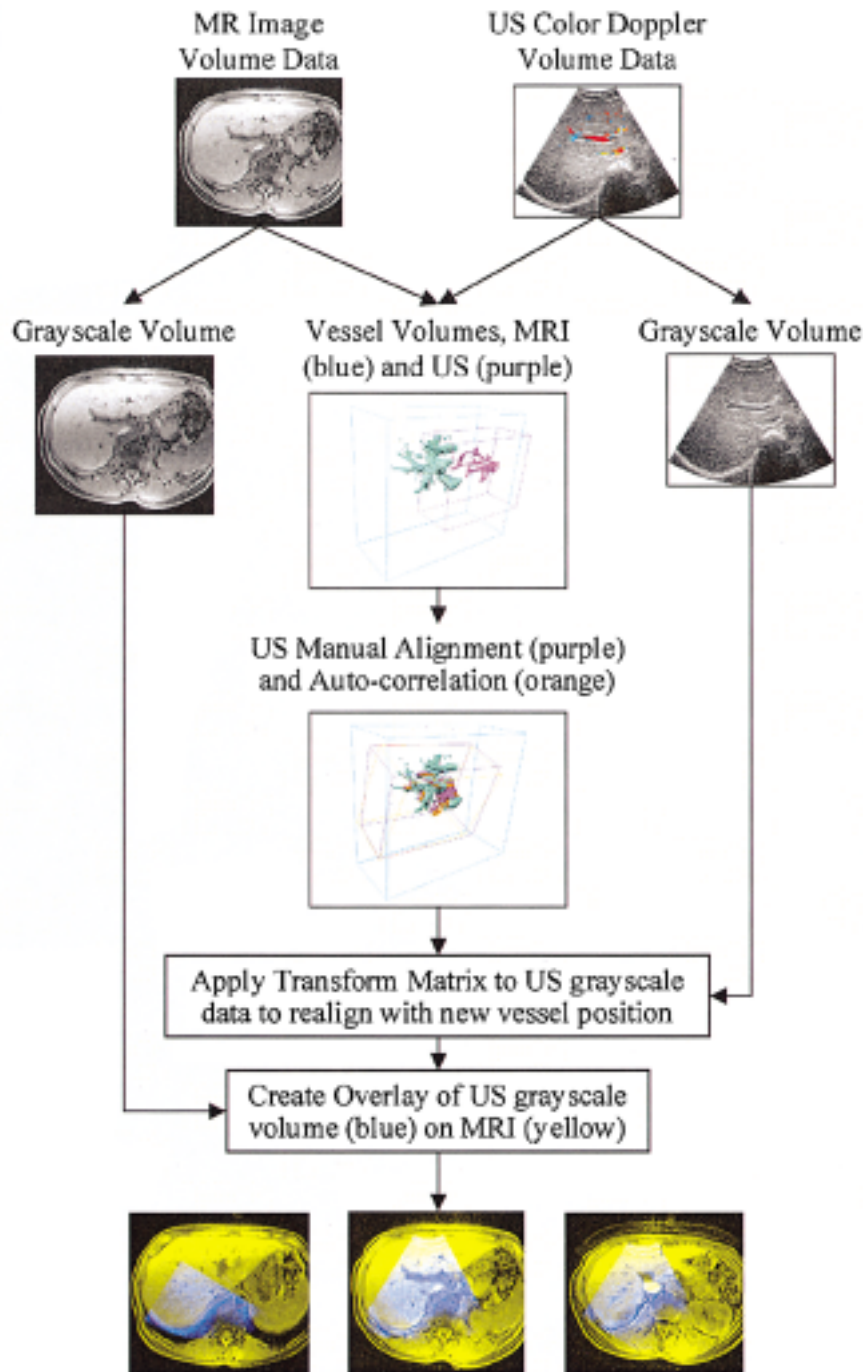


Fig. 4. Total 3-D fusion procedure (flowchart).

following sequence:  $Z$ - $Y$ - $X$  rotations,  $X$ - $Y$ - $Z$  translations. The best vessel overlap produced in the fine-tuning stage of the fusion process yields the largest of the normalized 3-D cross-correlation values. The rotation and translation of the US volume is mathematically described by a transformation matrix which is used to create the fusion display of the original grayscale medical images. Fig. 4 shows a pictorial flowchart of fusion steps for MRI and US volumes.

### III. RESULTS

Registration error is not simple to define and quantify for vessel segments. In previous work on framed fusion with fiducial markers, the

error is usually calculated as the RMS (root mean square) error on the distance of point-pair markers. However, vessel correlation uses no such point-pairs, so a different error metric must be used. In order to determine the quality of a fusion set, we can itemize maximum displacement (i.e., misregistration) of known boundaries of vessels and organs, or landmarks (the diaphragm), or internal calcifications if present. *In vivo* and phantom error results were obtained by inspecting fusion volume images.

Some potential sources of error arise from the 3-D acquisition system. The reconstructed US volume may be distorted in the  $Z$ -dimension if the US scanner frame rate and linear track speed are not calibrated or if the track is not held steady by the operator. Other sources of error may be caused by vessel segmentation and

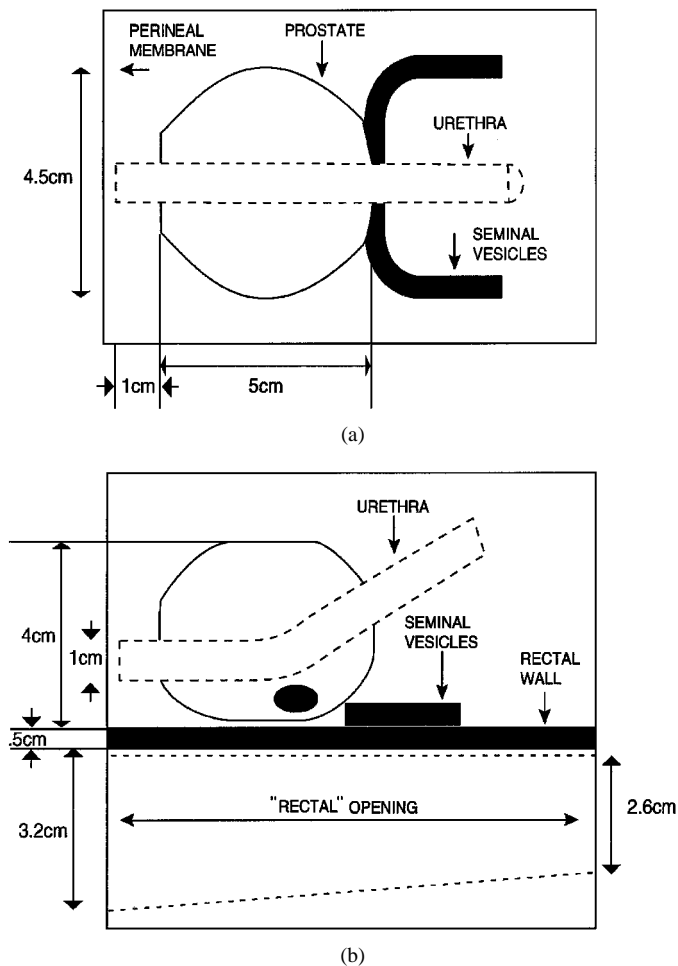


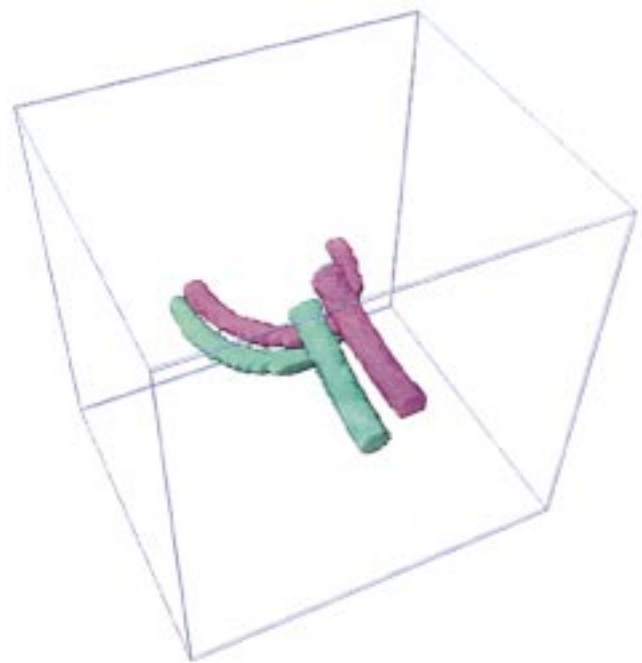
Fig. 5. CIRS prostate phantom diagram. This phantom was scanned with US and MRI for verification of the fusion algorithm. (a) Top view. (b) Side view.

reconstruction from Doppler US data. Doppler blooming (over-estimation of vessel size) and signal dropout from pulsatile flow may result in nonuniform or discontinuous vessel segments. Doppler signal strength is also affected by the interrogation angle to blood flow. Soft tissue deformations that deform vessel structures within organs can potentially add error to the final fusion result.

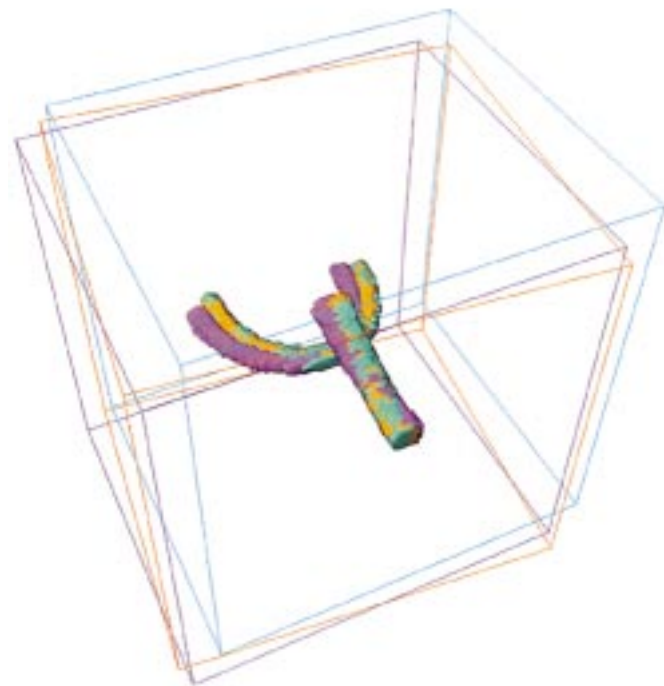
#### A. Phantom Studies

To verify the experimental methods and metrics, an initial study of MRI-MRI fusion of a prostate phantom was conducted. Two MRI volumes were acquired from the same phantom by shifting the phantom by  $5^\circ$  about the  $z$  axis. The phantom was fabricated to mimic the prostate, urethra and surrounding tissue (Fig. 5) [Computerized Imaging Reference Systems, Inc., Norfolk, VA]. The urethra and seminal vesicles served as vessel-like structures in the fusion algorithm. Fig. 6(a) shows the segmented urethra and seminal vesicles for both volumes. Fig. 6(b) shows the fixed MRI volume (blue) with the moveable volume before fusion (purple) and after fusion (orange). The displacement error, as measured from edges and landmarks in the fused data set, was less than 1 mm throughout the fused volume.

The next level of verification utilized MRI and US scans of the same prostate phantom. Since the phantom does not have an intrinsic Doppler signal, a low frequency "sonoelastic" vibration at 306 Hz was applied to obtain a volume image with color flow CINE [3], [4]. The prostate urethra was then segmented and used to fuse the US into the MRI volume.



(a)



(b)

Fig. 6. MRI scans of the prostate phantom. (a) Two MRI volumes were obtained with axial (blue) and oblique-axial (purple) orientations. Boxes denote volume boundaries, straight column is segmented urethra, and curved u-shaped tubes are segmented seminal vesicles. (b) The purple box and structure represent the initial manual alignment. The orange box and structure show the position of the final computer-generated alignment.

The measured displacement error within the internal phantom structures was less than 2 mm, despite inherent image distortion.

#### B. In Vivo Studies

The fusion algorithm was tested with two MRI scans of the forearm. One data set was obtained as direct axial images, and the second set

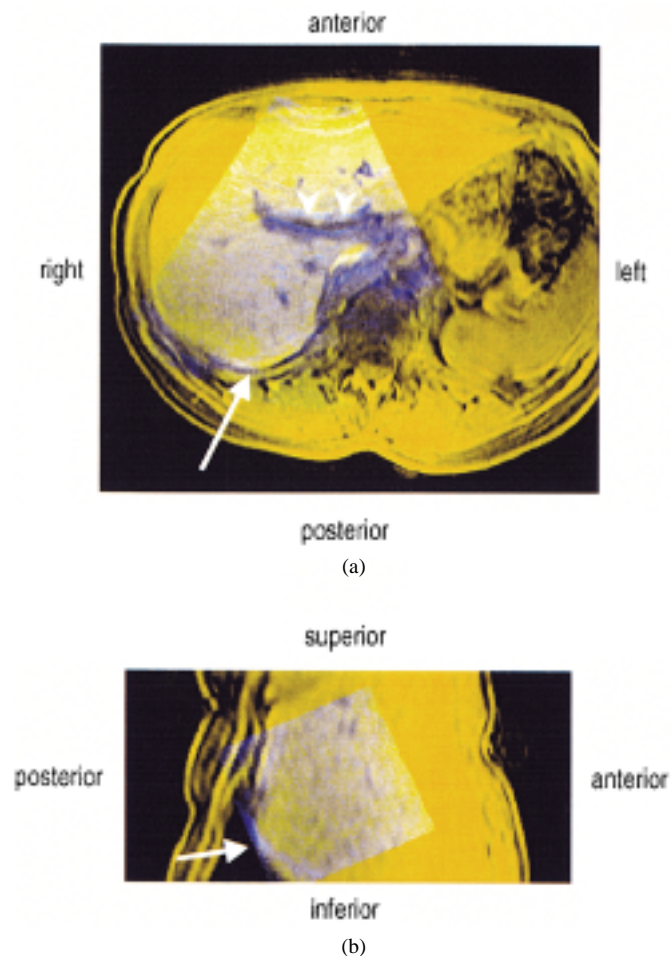


Fig. 7. MRI-US liver fusion. Fused grayscale volumes displayed with MRI in yellow and US in blue. (a) Fusion of axial MRI and oblique-axial US. Note diaphragm alignment (arrow) posteriorly, portal veins (arrowheads), anterior margin (US) depressed by transducer pressure. (b) Sagittal orientation confirms excellent diaphragm alignment (arrow) between US and MRI throughout the volume.

was obtained as oblique-axial images with a  $10^\circ$  shift off the  $z$  axis. The average displacement error, as measured from the skin surface, bone and internal landmarks was less than 1 mm.

Fusion of MRI and US data from the forearm was achieved using the brachial artery bifurcation as the common internal fiducial marker. The skin surface displacement error ranged from 4 mm to 8 mm. This comparatively large error is attributed to transducer pressure and the rotational movement of soft tissue around the radius and ulna as the arm was repositioned between scans (i.e., elbow flexed for US, elbow extended for MRI).

Finally, we fused MRI and curvilinear US volume scans of the liver. Fig. 7 shows axial and sagittal slices of the fused liver volumes with MRI (yellow) and US (blue). The displacement error was measured from the liver surface and vessel edge boundaries and ranged from 2 mm to 4 mm. Further examples of these fusion experiments are given at <http://www.ece.rochester.edu/users/porter/images/fusion/>.

An important clinical application of this fusion algorithm is to assist physicians with cancer treatment and followup assessment. Current tumor volume measurements are estimated in US by measuring the cross section in three (attempted) perpendicular image planes. Finding these exact image planes for followup comparisons over time (weeks, months, years) is difficult and may contribute to volume size errors. 3-D data sets are less prone to volume errors which result from arbitrary US scanning orientations.

#### ACKNOWLEDGMENT

The authors would like to thank S. Bileschi for his expert programming.

#### REFERENCES

- [1] M. L. Kessler, S. Pitluck, P. Petti, and J. R. Castro, "Integration of multimodality imaging data for radiotherapy treatment planning," *Int. J. Radiat. Oncol., Biol. Phys.*, vol. 21, pp. 1653–1667, 1991.
- [2] R. M. Haralick and L. G. Shapiro, "Image segmentation techniques," *Comput. Vis. Graph. Image Processing*, vol. 29, pp. 100–132, 1985.
- [3] L. Gao, K. J. Parker, S. K. Alam, and R. M. Lerner, "Sonoelasticity imaging: Theory and experimental verification," *J. Acoust. Soc. Amer.*, vol. 97, no. 6, pp. 3875–3886, 1995.
- [4] L. Gao, K. J. Parker, R. M. Lerner, and S. F. Levinson, "Imaging of the elastic properties of tissue—A review," *Ultrasound Med. Biol.*, vol. 22, no. 8, pp. 959–977, 1996.